Delayed-Stability Evaluation and Experimental Validation of Grid-Forming Inverter Dynamic Power-Hardware-in-the-Loop Tests

H. G. Oral, K. Prabakar, *Senior Member, IEEE,* D. M. Anand, *Member, IEEE,* S. Ganguly, *Member, IEEE,* and E. Mallada, *Senior Member, IEEE,*

***Abstract*—Grid-forming (GFM) inverters can sustain a large envelope of grid dynamics and provide resilience to outages and contingencies. Sophisticated control algorithms and the expanded functional use cases of GFM inverters do not have standardized testing protocols, which make their power hardware-in-the-loop (PHIL) validation particularly valuable. But, ensuring stable GFM PHIL tests is challenging as various experimental artifacts can be sources of destabilizing excitations for a GFM control loop. In this paper, we present methodologies to address challenges in performing GFM PHIL tests, and provide numerical analyses and experimental results that validate our approach. We first discuss the choice of empirical parameters, and tuning of closed-loop controllers that improve the stability and tracking performance of GFM PHIL experiments. We then provide analytical and numerical calculations evaluating the robustness of the closed-loop setup to experimental artifacts; particularly to delays, while accounting for destabilizing dynamic modes of the physical PHIL interconnection. Our experimental results validate closed-loop stability and tracking performance for PHIL tests of various operational modes of GFMs.**

***Index Terms*—power system test bed, hardware-in-the-loop, test and validation, grid forming.**

I. Introduction

Electrical power networks are estimated to host an increasing proportion of inverter-based resources (IBRs) in the coming decade, connecting solar photovoltaics (PV), wind, battery, fuel cell, and other hybrid generation sources. As an example, the North American Electric Reliability Corporation's long-term reliability assessment in 2021 notes that 504 GW of PV projects are in development to come online in the next 10 years [1], which is more than five times the approximately 97.2 GW of PV in operation as of 2022. Unlike synchronous generators, where the mechanical design strongly affects the closed-loop dynamics, the dynamic response of an IBR is predominantly a function of its software-defined control system and therefore can be continually modified or refined [2]. Practically all IBRs connected to the AC power system today operate in grid-following (GFL) mode [3], in which the angle, magnitude, and frequency of the grid-side AC voltage are tracked and current is generated to obtain the desired power output [4]. When constraints are violated, GFL inverters can disconnect from the grid, which may result in large-scale cascade tripping events, as documented in the analysis of a fault-induced cascade detachment of 1,200 MW of generating capacity in 2016 [5]. Alternately, the AC grid voltage can be established in a distributed fashion using grid-forming (GFM) inverters, which regulate their terminal voltage to balance generation and demand while sharing load between IBRs. Wide-scale deployment of GFM IBRs requires effective functional specifications for closed-loop control as well as for their integration with circuit protection, fault ride-through, and restoration systems. Further development of tools for modeling, simulation, and testing of GFM IBRs is also required to inform system designers and to standardize GFM capabilities and operations [6].

Power-hardware-in-the-loop (PHIL) tests—where *real* inverters interact with digitally simulated grid conditions in real time—are currently the industry benchmark for evaluating GFL inverters [7], [8], and they enable the rapid iteration of test scenarios that is needed to keep pace with innovation in inverter technology [9]. Also, reliable and repeatable PHIL tests are noted to lead to better technical standards for GFM inverters [10], [11], and repeatability of these tests are contingent upon the assessment of stability constraints imposed by experimental tools and the hardware under test (HUT). Stability constraints for dynamic testing of GFL inverters have been studied extensively [12]; however, best practices for that of GFM inverters with droop regulators are still being developed. Ensuring the stability of GFM inverter PHIL tests is challenging because the dynamic modes associated with various components of the PHIL setup (e.g., pulse width modulation (PWM) switching mechanism, controlled voltage source-GFM inverter interconnection line) may be a source of destabilizing excitations for the dynamic AC voltage control loop of a GFM inverter. Furthermore, measurement and computation delays inherent to the experimental setup can further degrade stability margins of the GFM inverter control loop.

In this paper, we present our experimental approaches to mitigate these challenges; and numerical analyses and experimental results that validate these approaches for PHIL testing of GFM inverters. Particularly, we first discuss the empirical choice of line parameters that yields a stable hardware interconnection for PHIL experiments. Then, we outline our implementation of closed-loop controllers for improving tracking accuracy and mitigating inherent experimental delays. We validate our approach by first deriving the overall closed-

H. G. Oral is with NIST and Johns Hopkins University, {hasangiray.oral@nist.gov, giray@jhu.edu}.

K. Prabakar and S. Ganguly are with NREL, {kumaraguru.prabakar, subhankar.ganguly}@nrel.gov.

D. M. Anand was with NIST and Johns Hopkins University.

E. Mallada is with Johns Hopkins University, mallada@jhu.edu.

loop dynamics including the GFM inverter droop response, the tracking controller, a reduced-order model of the interconnection line, and measurement and computation delays; and then using this model to perform a numerical stability analysis utilizing a frequency domain method for neutral time-delayed systems (NTDS). Our results provide insights into the role of delays in tracking performance and stability of GFM PHIL experiments and qualitatively demonstrate the impact of the line inductance on delay robustness. Finally, we present results from our experiments in various GFM and GFL operational modes that demonstrate the efficacy of the implementation of our PHIL test setup.

In Section II, we outline the differences and challenges in performing PHIL tests on GFM inverters compared to GFL inverters. In Section III, we describe the key components of our PHIL setup that will be analyzed in the sequel for tracking performance and stability. In sections IV and V, we provide derivations of our analytical model and present our numerical results. In Section VI, we present experimental results that validate our approach. Section VII concludes the paper.

II. Background

In this section, we outline some of the practical challenges in implementing a PHIL test setup and some of the modifications that are commonly employed to improve accuracy and stability. This background is intended to motivate our analysis to evaluate modifications and compensation schemes to improve the performance of dynamic PHIL experiments.

A. Admissibility of Inverter Parameters in Steady State

First, we consider a PHIL test for a GFL inverter in steady state. As a reminder, a GFL inverter acts as a current source, injecting the desired magnitude of the active and reactive power into a point of interconnection with an already extant grid. The steady-state test for a GFL inverter is reduced to verifying that the inverter under test accurately delivers the requested levels of active (P) and reactive power (Q) while tracking (or following) the voltage at the point of interconnection and abiding by the grid interconnection constraints. This test can be conducted using the simplified PHIL setup shown in Figure 1, where independent measurements of the inverter interconnection bus variables (V_1, I, ϕ) taken at different set points for the inverter output (P, Q) and at different values for the grid state (V_2) serve to verify the inverter operation via the AC power flow relations: $P = V_1 I \cos\phi$ and $Q = V_1 I \sin\phi$.

The steady-state solution for the inverter terminal voltage ($V_1 \angle \delta$) must satisfy not only the relationship between the injected powers and the bus voltages but also the nonlinear impact of the impedance $Z_h = R + \mathrm{j}X$. The complex valued Z_h is an artifact of the test hardware used for the experiment,

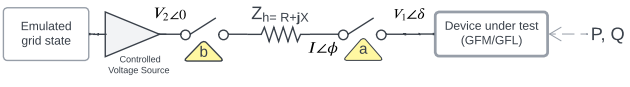

Fig. 1: Ideal setup

and it is determined by the electrical connections between the controlled voltage source and the point of interconnection to the inverter under test. This line impedance, once characterized, can be compensated for in the measurements obtained from the experiment; however, this impedance is a significant contributor to the conditions for voltage stability of the abstract two-bus power system represented in Figure 1 [13].

Rewriting the AC power relations to include the parameters of the test setup (Z_h) and the emulated grid state (V_2), we get:

$$\begin{aligned} P &= \frac{V_1}{Z_h^2}\left[V_1 R - V_2(R\cos\delta - X\sin\delta)\right] \\ Q &= \frac{V_1}{Z_h^2}\left[V_1 X - V_2(X\cos\delta + R\sin\delta)\right] \end{aligned} \tag{1}$$

Note that (1) comports with the intuition that both the active and reactive power injections from the inverter increase in proportion to the difference between the inverter terminal voltage, V_1, and the emulated grid voltage, V_2 (for small angles); therefore, the controlled voltage source can be used to emulate different grid impedance conditions by changing V_2. But a lower limit to the effective grid load impedance is reached at the maximum power point for the circuit where the voltage drop across Z_h would counterintuitively result in reducing the active power with a decrease in the emulated load impedance. We can demonstrate this by combining the equations in (1) and reordering the terms to get an algebraic relation for the inverter terminal voltage, V_1, shown in (2):

$$V_1^4 - \left(2(RP + XQ) + V_2^2\right) V_1^2 + \left(P^2 + Q^2\right) Z_h^2 = 0 \tag{2}$$

Equation (2) only yields distinct real roots for V_1 (indicating admissible voltage solutions) when the discriminant satisfies the condition in (3):

$$V_2^4 + 4(PR + QX)V_2^2 - 4(PX - QR)^2 > 0 \tag{3}$$

Although (3) is not an explicit solution for voltage stability, note that this condition expresses voltage stability in terms of variables that are under the control of the PHIL test setup, i.e., the active and reactive power set points (P, Q), the line impedance (R, X), and the voltage of the controlled voltage source (V_2). We can see that the discriminant is positive only when the emulated grid voltage $V_2 > 0$ and that the practical lower bound on V_2 is determined by the primary destabilizing term $-4(PX - QR)^2$. This stability condition is similar in principle to the line loadability constraints associated with transmission lines with high X/R ratios, and it highlights the practical limits on the power capacity of a given test setup. The stability condition also demonstrates the interesting dependencies associated with the AC power flow, such as the stability improvement awarded by reactive power injections over resistive lines. Although the condition in (3) applies to the steady-state admissibility of PHIL experiments on GFM inverters as well, a GFM inverter is expected to maintain/balance the grid frequency and its voltage V_1 while the constraints on the controlled voltage source are relaxed to emulate a desired grid load impedance ($\frac{V_2^2}{S_g}$) where $S_g = \sqrt{(P^2 + Q^2)}$ is the complex grid load. We can refactor (2) to observe that the

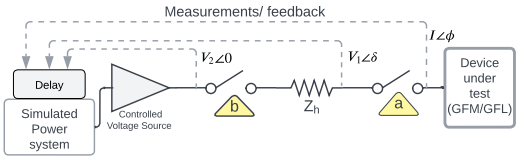

Fig. 2: PHIL setup showing a closed-loop experiment

admissibility conditions on V_1 are easier to achieve because a real solution for V_2 exists when the conditions in (4) are met.

$$V_1^4 + (S_g Z_h)^2 - 2(PR + QX)V_1^2 > 0 \tag{4}$$

The latter observation comports with anecdotal observations in our PHIL testing where we observed that the stability of PHIL experiments appears to become marginal when operating at relatively high values for P and small values for Q.

B. Considerations in Testing Dynamic Response of Inverters

Developing stability conditions for a PHIL test setup under dynamic conditions is challenging because the dynamic modes that affect the stability of the PHIL setup cannot be ranked in significance based on timescale or bandwidth, i.e., there are cases where fast transients that are considered outside the bandwidth of interest for the experiment can compromise the stability of the setup [14]. A common example of such a case is the role of electromagnetic transients associated with pulse width modulation (PWM) on PHIL stability. These aliased artifacts are relevant to PHIL experiments as both the inverter under test and the controlled voltage source modulate the DC power to synthesize the AC waveforms. The interactions between these two switching power converters have been observed to interact with line dynamics as well as the tracking and sensing loops within the inverters under test [15].

As shown in Figure 1, we can inspect the stability conditions for the two-bus system comprising a GFM inverter; the coupling impedance, Z_h; and an infinite bus at frequency ω_0 with voltage ($V_2\angle 0$). The stability of the two-bus system following a connection event, i.e., closure of breakers a and b, is determined by the GFM inverter droop response—the volt-VAR ($V_1 - Q$) and the frequency-watt ($\omega - P$) dynamic response of the inverter. The authors in [14] show that stability margins for droop dynamics strongly depend on the interconnection line dynamics if the inductance-resistance ratio L/R is on the same order as the time constant of the nominal AC response. Three-phase resistance and inductance measurements of the PHIL interconnection line are given in Figure 3. Based on these measurements, $R/L \approx 73$ Hz, which is on the same order as the nominal frequency $f_0 = 60$ Hz. We incorporated this factor into our PHIL setup, as discussed later in this paper.

Consider the actuation of the switches labeled *a* and *b* in Figure 1. These two switches represent an in-feed breaker/contactor and a grid/off-grid transfer switch, respectively. Although breakers/contactors are often external to an inverter, they represent an important dynamic interaction for an inverter in the field and are therefore often included in the PHIL setup to evaluate the transient response and steady-state convergence properties of the inverter to disconnection and reconnection events. Even in this simple case, it is important to establish, mitigate, and compensate for the response of the PHIL test equipment, complete with interconnection impedances to switching excitation, before collecting data on the response of the inverter control system.

The closed-loop operation in a PHIL experiment is illustrated in Figure 2, where measurements from the inverter under test are fed back as inputs to a model of a power system (shown by the gray dashed lines), which, in turn, is simulated in real time so that the output to the controlled voltage source reflects the grid dynamics of interest. Clearly, delays in the feedback path directly affect the accuracy and stability of this closed-loop system. Common sources of delays include measurement delays associated with the analog to digital conversion and latency caused by the nontrivial computation time needed to simulate the response of a power system; and these sources are abstracted as an aggregate delay mapping in Figure 2.

Under steady-state conditions, a common strategy used to compensate for feedback delays is to assume that the delay introduces a corresponding retardation of the voltage angle reference produced by the voltage source, $V_2\angle\epsilon$. Assuming the experiment runs at close-to-nominal grid frequency and experiences near-constant feedback delays, the voltage reference angle, ϵ, can be corrected in the software. When performing the dynamic testing of GFL inverters, these delays are characterized as introducing a phase lag in the closed-loop model, and compensation can be applied by inserting an appropriately tuned phase lead [16], [17].

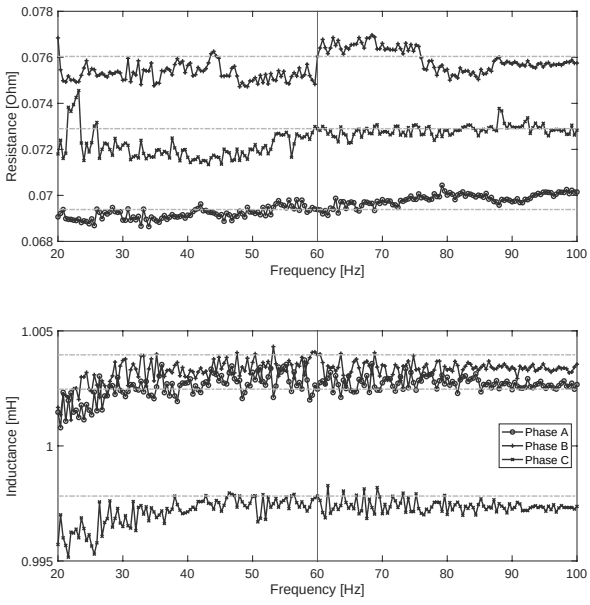

Fig. 3: Resistance and inductance measurements

III. Power-Hardware-in-the-Loop Setup

In this section, we present the building blocks of our PHIL test setup and elaborate on how they address the considerations

in dynamic testing of GFM inverters, which we outlined in Section II-B. As shown in Figure 4, which provides a complete schematic of our closed-loop PHIL experiments, hardware components are mirrored in the digital real-time simulation domain so as to emulate PHIL testing conditions. The constituents of these two domains are described first. Note that labels *a* and *b* in Figure 2 also refer to the same actuation switches in Figure 4 wherein signal measurement channels are numbered for reference. Then, we overview the compensation scheme implemented in order to sustain closed-loop stability and tracking accuracy.

A. Hardware Setup

Power-Hardware-Under-Test: Our work targets a commercially available, off-the shelf GFM inverter designed to interface fuel cells as the power-hardware-under-test, the output of which is taken from node 1 in Figure 4. The intellectual property of the lower-level control structure is not available for modeling the inverter in a digital real-time simulation; therefore, a PHIL setup needs to be used to evaluate the inverter performance under different modes of operation. A controllable DC supply energizes the inverter under test.

Controllable DC supply: We use a DC battery emulator, the Aerovironment AV 900, operating in constant voltage mode to supply DC power to the fuel cell inverter. Key settings include a voltage set point of 450 V DC (with trip settings at 500 V DC), a DC current limit of 250 A DC, and a power limit of 112.5 kW. These configurations ensure efficient testing and adherence to the fuel cell inverter and laboratory AC and DC bus specifications.

Grid Emulator - Controllable AC supply: A controllable AC supply rated at 270 kVA AC is used as the grid emulator and interfaces the inverter at node 7 in Figure 4. The grid emulator receives an analog input that is filtered by the compensation and real-time simulation domains (node 6) and amplifies it to represent the bus voltage of the power system model at node 7. Notably, the grid emulator magnifies a 7 V root-mean-square (RMS) AC voltage to a 300 V RMS AC voltage. We set the protection limit of the grid emulator at 300 V maximum and 150 A for bidirectional current.

At the outset, sound engineering design practices are called for when selecting the controllable voltage source and the corresponding amplifier with regard to their saturation limits, frequency bandwidths, response times, and harmonic distortions. Calibration is often required to address bias in the amplifier gain and to compensate for the input/output impedance of the interface hardware. These experimental considerations are shared among a wide range of PHIL testing applications and are enumerated in standards aimed at improving PHIL testing practices across the industry. A summary of these standardization efforts is presented in [18].

Series inductor: The series inductor is a commercial off-the-shelf device with an inductance of 1 millihenry (mH) in each phase (see Figure 3). The series inductor is rated for operation of 120 A of current in each phase with a rated line-to-neutral voltage of 277 V (480 V line-to-line RMS). As we will show in the sequel, this inductance value provides a stable interconnection between the inverter and the controllable AC supply and robustness to loop delays during PHIL tests.

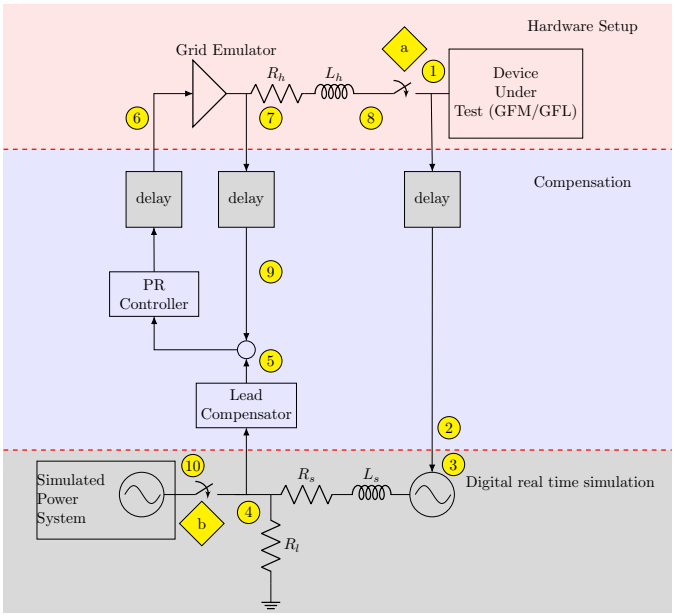

Fig. 4: PHIL laboratory hardware setup

B. Digital Real-Time Simulation (DRTS)

We use a commercial Real-Time Digital Simulator (RTDS) for computations in the simulation domain, which were performed at 50 microseconds (μs) and at 100 μs. These two time steps were taken as examples to demonstrate that the proposed approach works in multiple time step configurations.

Software model of the power system: Node 10 in Figure 4 refers to the output of the power system model used in the DRTS platform. This model is a simplified version of a microgrid. We use resistive, inductive, and capacitive loads to represent typical loads in a microgrid system. The series resistance-inductance pair (R_s, L_s) used here replicates that of the hardware setup. Further details of DRTS implementation are presented in [17].

C. Compensation Scheme

As shown in Figure 4, closed-loop operation is sustained by a digital compensation scheme that interconnects the hardware setup to the DRTS domain. The purpose of compensation is two-fold; it is to improve the tracking performance of the grid-emulator and to compensate for loop delays that may degrade stability margins and tracking accuracy.

Lead Compensator: A standard lead compensator is used to compensate for loop delays incurred in the simulated grid signal, which is taken at node 4 in Figure 4. This loop delay consists of the delay between nodes 1 and 3 in Figure 4 and computation time due to real-time simulation. Compensator parameters are tuned according to this aggregate delay value.

Tracking Controller: Tracking performance is improved using a properly tuned resonant controller [19]. A resonant controller's action on sinusoidal inputs can be interpreted as

an analogous integral controller's action on a step input. The goal is to reduce the error between signals 5 and 7 in Figure 4. In addition to reducing tracking error, the resonant controller provides some degree of delay robustness around the nominal operation frequency as we will demonstrate in the sequel.

IV. Delay-Independent Stability Of The Tracking Loop

In this section, we investigate the stability of the tracking (resonant controller) loop, which we analyze independently for simplicity, proving delay-independent stability for a frequency interval that contains the nominal operation frequency. The tracking loop is given in Figure 4 between points 5 and 7. The transfer function of the resonant controller is given by [19]:

$$T_R(s) = \frac{k_R s}{s^2 + b_R s + \omega_0^2},$$

where $k_R > 0$ is the controller gain, and setting b_R to a positive value renders a finite bandwidth around the operating frequency, ω_0, as $T(j\omega_0) = \frac{k_R}{b_R}$. For our application, we set approximately $\frac{k_R}{b_R} \approx 2f_0 = 120$ Hz.

The grid emulator is characterized as a first-order filter with delay [17]:

$$T_{GE}(s) = e^{-s\tau_f} \frac{\omega_g}{s + \omega_g},$$

where ω_g is the cutoff frequency, and τ_f is an aggregated delay in the forward path that includes the grid emulator and real-time simulation delays. The closed-loop transfer function is:

$$\begin{aligned} T_{tracking}(s) &= \frac{T_R(s)T_{GE}(s)}{1 + T_R(s)T_{GE}(s)e^{-s\tau_b}} \\ &= \frac{\omega_g k_R s e^{-s\tau_f}}{(s^2 + b_R s + \omega_0^2)(s + \omega_g) + k_R s \omega_g e^{-s(\tau_f + \tau_b)}}, \end{aligned} \tag{5}$$

where τ_b denotes the delay in the feedback. The delay term $e^{-s\tau_f}$ can be interpreted as an input delay, so it will be lumped into the delay in the simulation, which is addressed by a lead compensator. We evaluate the stability of the tracking loop by computing the roots of the characteristic polynomial of (5). First, we certify the stability as if there was no delay, and then we look for possible imaginary axis crossings of poles due to a delay. Using a standard approach [20], for a practical interval of frequencies, we show that the tracking loop is delay-independent stable. For $\tau_f = \tau_b = 0$, the characteristic equation is given by:

$$s^3 + a_2 s^2 + a_1 s + a_0 = 0,$$

where $a_2 = b_R + \omega_g$, $a_1 = \omega_0^2 + (b_R + k_R)\omega_g$ and $a_0 = \omega_0^2 \omega_g$. The roots are on the open left-half plane if and only if $a_i > 0$ for $i = 0, 1, 2$ and $a_2 a_1 > a_0$ by the Routh-Hurwitz stability criterion. All a_i coefficients are positive, and the latter condition holds true because

$$\begin{aligned} &(b_R + \omega_g)(\omega_0^2 + (b_R + k_R)\omega_g) > \omega_0^2 \omega_g, \quad \text{i.e.,} \\ &b_R \omega_0^2 + (b_R + k_R)(b_R \omega_g + \omega_g^2) > 0. \end{aligned}$$

Then, we consider $\tau_f + \tau_b > 0$ and substitute $s = j\omega$ in the characteristic equation of (5) to evaluate possible imaginary axis crossings of roots:

$$\begin{aligned} c(j\omega) &:= \frac{\omega^2 - (\omega_0^2 + (b_R + k_R)\omega_g)}{k_R \omega_g} + j \frac{\omega_0^2 \omega_g - \omega^2 (b_R + \omega_g)}{k_R \omega_g \omega} \\ &= e^{-j\omega(\tau_f + \tau_b)}. \end{aligned} \tag{6}$$

Note that setting $\Re(c(j\omega)) < -1$ guarantees that the equality in (6) does not hold because the right-hand side has a magnitude of 1, and therefore no poles cross the imaginary axis. To find an upper bound on ω that satisfies this condition, set $\Re(c(j\omega)) = -1$, which leads to:

$$\frac{\omega^2 - \omega_0^2}{\omega_g} - b_R = 0 \quad \Rightarrow \quad \omega = \sqrt{\omega_0^2 + b_R \omega_g}.$$

Because $\Re(c(j\omega))$ is monotonically increasing in ω, $\Re(c(j\omega)) < -1$ holds if:

$$\omega < \sqrt{\omega_0^2 + b_R \omega_g},$$

which is sufficient for the delay-independent stability of the tracking loop. Note that increasing b_R trades off tracking accuracy (a smaller open-loop gain at the nominal frequency, ω_0) for delay robustness because the delay-independent stable region can be expanded as b_R is increased.

V. Impact of Line Dynamics and Interface Delay

In this section, first, we construct a simple two-voltage source model that includes transient dynamics of the hardware interconnection line and data transfer delays that arise in the closed-loop hardware simulation interface. Under simplifying assumptions, we evaluate how closed-loop stability is impacted by line dynamics and delays.

A. Power Flow due to a First-Order Approximation of Line Dynamics With Delay

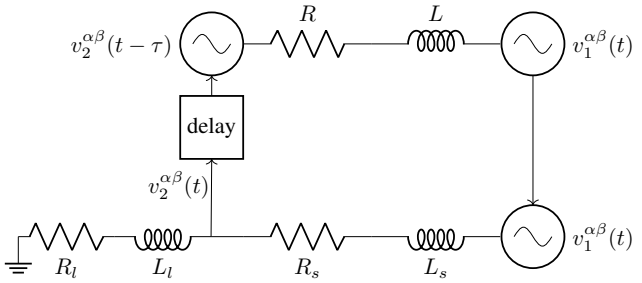

Fig. 5: Hardware simulation interconnection with delay

We define the balanced three-phase voltage signals in the stationary $\alpha\beta$ coordinates as:

$$v_i^{\alpha\beta}(t) := V_i(t) e^{j\Phi_i(t)} =: v_i(t) e^{j\omega_0 t}, \tag{7}$$

where $\Phi_i(t) = \phi_i(t) + \omega_0 t$. Note that the definition in (7) also implies a phasor form given in terms of the phase angle $\phi_i(t)$ and RMS voltage magnitude, $V_i(t)$, as $v_i(t) = V_i(t) e^{j\phi_i(t)}$. We assume that the system has a sinusoidal equilibrium expressed as $\Phi_i(t) \to \omega_0 t + \phi_i^*$ and $V_i(t) \to V_i^*$ as $t \to \infty$

with constant ϕ_i^* and V_i^*. We use this set of definitions for voltage source 1 (the device under test—GFM inverter) and voltage source 2 (grid emulator), which are interconnected with a line with resistance, R, and inductance, L, as given in Figure 5. The line dynamics are given by:

$$L\frac{di_{12}^{\alpha\beta}}{dt} = -Ri_{12}^{\alpha\beta}(t) + v_1^{\alpha\beta}(t) - v_2^{\alpha\beta}(t-\tau),$$

where the induced current would be of the form $i_{12}^{\alpha\beta}(t) := i_{12}(t)e^{j\omega_0 t}$, and we introduce an input delay, τ, to voltage source 2. Then, using the definitions in (7), the line dynamics can be written in a coordinate frame that rotates as $e^{j\omega_0 t}$:

$$\begin{aligned} L\frac{di_{12}}{dt} + (R + j\omega_0 L)i_{12}(t) &= v_1(t) - v_2(t-\tau)e^{-j\omega_0\tau} \\ &=: \Delta v_{12}(t,\tau) \end{aligned} \tag{8}$$

Taking the Laplace transform of (8) gives:

$$i_{12}(s,\tau) = \frac{\Delta v_{12}(s,\tau)}{Ls + R + j\omega_0 L} =: i_{12}^0(s,\tau)\frac{1}{\frac{Ls}{R+j\omega_0 L}+1},$$

where $i_{12}^0(s,\tau) = \frac{\Delta v_{12}(s,\tau)}{R+j\omega_0 L}$ is the zeroth-order (quasi-static) phasor current. Using an argument similar to the one in [14], we assume a sufficiently small $|\frac{Ls}{R+j\omega_0 L}|$ that allows a first-order Taylor approximation:

$$i_{12}(s,\tau) \approx i_{12}^0(s,\tau)\left(1 - \frac{L}{R+j\omega_0 L}s\right),$$

which can be expressed in the time domain as:

$$\begin{aligned} i_{12}(t,\tau) &\approx \frac{\Delta v_{12}(t,\tau)}{R+j\omega_0 L} - \frac{L}{(R+j\omega_0 L)^2}\frac{d}{dt}\Delta v_{12}(t,\tau) \\ &= \frac{v_1(t) - v_2(t-\tau)e^{-j\omega_0\tau}}{R+j\omega_0 L} \\ &\quad - \frac{L}{(R+j\omega_0 L)^2}\left(\dot{v}_1(t) - \dot{v}_2(t-\tau)e^{-j\omega_0\tau}\right) \end{aligned}$$

The instantaneous complex power can then be computed as:

$$\begin{aligned} p_{12}(t) &= v_1(t)i_{12}(t)^H \\ &\approx v_1(t)\Big[(G-jB)(v_1(t)^H - v_2(t-\tau)^H e^{j\omega_0\tau}) \\ &\quad - (G'+jB')\left(\dot{v}_1(t)^H - \dot{v}_2(t-\tau)^H e^{j\omega_0\tau}\right)\Big] \\ &= V_1(t)\Big[(G-jB)(V_1(t) - V_2(t-\tau)e^{j\theta_{12}(t,\tau)}) \\ &\quad - (G'+jB')\Big(\dot{V}_1(t) - \dot{V}_2(t-\tau)e^{j\theta_{12}(t,\tau)} \\ &\quad - jV_1(t)\dot{\phi}_1(t) + jV_2(t-\tau)\dot{\phi}_2(t-\tau)e^{j\theta_{12}(t,\tau)}\Big)\Big] \end{aligned} \tag{9}$$

where $\theta_{12}(t,\tau) := \phi_1(t) - \phi_2(t-\tau) + \omega_0\tau$, the complex conjugation is denoted by superscript 'H,' and we use the definitions:

$$\begin{aligned} G &:= \frac{R}{R^2+\omega_0^2L^2}, \quad B := -\frac{L\omega_0}{R^2+\omega_0^2L^2}, \\ G' &:= \frac{L(R^2-\omega_0^2L^2)}{(R^2+\omega_0^2L^2)^2}, \quad B' := \frac{2RL^2\omega_0}{(R^2+\omega_0^2L^2)^2}. \end{aligned}$$

We then linearize (9) with respect to the variable $x(t,\tau) = \begin{bmatrix} x_1(t) & x_2(t-\tau)\end{bmatrix}^T$ with $x_i(t) := \begin{bmatrix}\phi_i(t) & \dot{\phi}_i(t) & V_i(t) & \dot{V}_i(t)\end{bmatrix}$, and around an equilibrium point $x^* = \begin{bmatrix}x_1^* & x_2^*\end{bmatrix}^T$ with $x_i = \begin{bmatrix}\phi_i^* & 0 & V_i^* & 0\end{bmatrix}$:

$$\begin{aligned} \delta p_{12}(t,\tau,x^*) &=: \delta P_{12}(t,\tau,x^*) + j\delta Q_{12}(t,\tau,x^*) \\ &\approx (\nabla_x\, p_{12}(t,\tau)|_{x=x^*})^T\, \delta x(t,\tau) \\ &= \begin{bmatrix} -j(G-jB)V_1^*V_2^*e^{j(\phi_{12}^*+\omega_0\tau)} \\ j(G'+jB')V_1^{*2} \\ (G-jB)(2V_1^* - V_2^*e^{j(\phi_{12}^*+\omega_0\tau)}) \\ -(G'+jB')V_1^* \\ j(G-jB)V_1^*V_2^*e^{j(\phi_{12}^*+\omega_0\tau)} \\ -j(G'+jB')V_1^*V_2^*e^{j(\phi_{12}^*+\omega_0\tau)} \\ -(G-jB)V_1^*e^{j(\phi_{12}^*+\omega_0\tau)} \\ (G'+jB')V_1^*e^{j(\phi_{12}^*+\omega_0\tau)} \end{bmatrix}^T \begin{bmatrix}\delta x_1(t)^T \\ \delta x_2(t-\tau)^T\end{bmatrix}, \end{aligned} \tag{10}$$

where $\phi_{12}^* := \phi_1^* - \phi_2^*$, P_{12}, and Q_{12}, respectively, denote the real and reactive power; and 'δ' in front of a variable indicates its difference from the equilibrium. Next, we provide the droop dynamics of the device under test, the GFM inverter, due to the first-order approximation of the power flow with a delay in (10).

B. Droop Dynamics With Line Dynamics and Input Delay

Then, the linearized droop dynamics of the first voltage source (inverter) interconnected with the second voltage source (grid simulator) are given by:

$$\begin{aligned} \delta\dot{\phi}(t) &\approx \delta\omega(t) \\ \sigma\delta\dot{\omega}(t) &\approx -\delta\omega(t) - d_p\delta P(t,\tau) \\ \sigma\delta\dot{V}(t) &\approx -\delta V(t) - d_q\delta Q(t,\tau) \end{aligned}$$

Here, we use a first-order approximation of the line dynamics. We drop the subscript enumeration from the variables in the closed-loop expressions because these variables will only pertain to the inverter once we perform the subsequent closed-loop substitutions. We make the following assumption pertaining to the parameters of the simulated line and load.

Assumption 1. *The difference between the respective inductance-to-resistance ratios of the simulated line and the simulated load is small, i.e.:*

$$\left|\frac{L_s}{R_s} - \frac{L_l}{R_l}\right| < \rho$$

where ρ is a small nonnegative number. This implies that:

$$|v_2 - \gamma v_1| \to 0$$

as $\rho \to 0$, where $\gamma = \frac{R_l}{R_s+R_l}$ (See Appendix A for derivation).

This assumption, though it restricts our analysis to a fixed real-to-reactive load ratio, provides a reduction in the model order and thereby facilitates gaining useful insight into the stability properties of the GFM inverter testing. We highlight that test cases involving arbitrary values of apparent power are covered by this assumption as long as real and reactive loads scale according to the fixed ratio. For simplicity, we choose

the phase angle equilibrium points as $\phi_{12}^* = 0$, which, together with Assumption 1, leads to $V_2^* = \gamma V_1^*$, $\delta V_2 \approx \gamma \delta V_1$ and $\delta\phi_2 \approx \delta\phi_1$ (see Appendix B for derivation). After substituting for these variables (and dropping the subscript index for the inverter parameters), we obtain the following power flow expressions:

$$\delta P(t,\tau) \approx$$
$$\begin{bmatrix} -\gamma V^{*2}(B\cos(\omega_0\tau) - G\sin(\omega_0\tau)) \\ -V^{*2}B' \\ GV^*(2-\gamma\cos(\omega_0\tau)) - B\gamma V^*\sin(\omega_0\tau) \\ -V^*G' \\ \gamma V^{*2}(B\cos(\omega_0\tau) - G\sin(\omega_0\tau)) \\ \gamma V^{*2}(B'\cos(\omega_0\tau) + G'\sin(\omega_0\tau)) \\ -\gamma V^*(G\cos(\omega_0\tau) + B\sin(\omega_0\tau)) \\ \gamma V^*(G'\cos(\omega_0\tau) - B'\sin(\omega_0\tau)) \end{bmatrix}^T \begin{bmatrix} \delta\phi(t) \\ \delta\dot{\phi}(t) \\ \delta V(t) \\ \delta\dot{V}(t) \\ \delta\phi(t-\tau) \\ \delta\dot{\phi}(t-\tau) \\ \delta V(t-\tau) \\ \delta\dot{V}(t-\tau) \end{bmatrix}$$
$$\delta Q(t,\tau) \approx$$
$$\begin{bmatrix} -\gamma V^{*2}(G\cos(\omega_0\tau) + B\sin(\omega_0\tau)) \\ V^{*2}G' \\ -BV^*(2-\gamma\cos(\omega_0\tau)) - G\gamma V^*\sin(\omega_0\tau) \\ -V^*B' \\ \gamma V^{*2}(G\cos(\omega_0\tau) + B\sin(\omega_0\tau)) \\ -\gamma V^{*2}(G'\cos(\omega_0\tau) - B'\sin(\omega_0\tau)) \\ \gamma V^*(B\cos(\omega_0\tau) - G\sin(\omega_0\tau)) \\ \gamma V^*(B'\cos(\omega_0\tau) + G'\sin(\omega_0\tau)) \end{bmatrix}^T \begin{bmatrix} \delta\phi(t) \\ \delta\dot{\phi}(t) \\ \delta V(t) \\ \delta\dot{V}(t) \\ \delta\phi(t-\tau) \\ \delta\dot{\phi}(t-\tau) \\ \delta V(t-\tau) \\ \delta\dot{V}(t-\tau) \end{bmatrix} \tag{11}$$

Taking $V^* = V_b$ (1 per unit (pu)) and normalizing the voltage magnitude as $\delta U = \frac{\delta V}{V_b}$, where V_b denotes the base voltage magnitude, we state the per-unit power expressions as:

$$\delta P_{\text{pu}}(t,\tau) \approx$$
$$\begin{bmatrix} -\gamma(B\cos(\omega_0\tau) - G\sin(\omega_0\tau)) \\ -B' \\ G(2-\gamma\cos(\omega_0\tau)) - B\gamma\sin(\omega_0\tau) \\ -G' \\ \gamma(B\cos(\omega_0\tau) - G\sin(\omega_0\tau)) \\ \gamma(B'\cos(\omega_0\tau) + G'\sin(\omega_0\tau)) \\ -\gamma(G\cos(\omega_0\tau) + B\sin(\omega_0\tau)) \\ \gamma(G'\cos(\omega_0\tau) - B'\sin(\omega_0\tau)) \end{bmatrix}^T \begin{bmatrix} \delta\phi(t) \\ \delta\dot{\phi}(t) \\ \delta U(t) \\ \delta\dot{U}(t) \\ \delta\phi(t-\tau) \\ \delta\dot{\phi}(t-\tau) \\ \delta U(t-\tau) \\ \delta\dot{U}(t-\tau) \end{bmatrix}$$
$$\delta Q_{\text{pu}}(t,\tau) \approx$$
$$\begin{bmatrix} -\gamma(G\cos(\omega_0\tau) + B\sin(\omega_0\tau)) \\ G' \\ -B(2-\gamma\cos(\omega_0\tau)) - G\gamma\sin(\omega_0\tau) \\ -B' \\ \gamma(G\cos(\omega_0\tau) + B\sin(\omega_0\tau)) \\ -\gamma(G'\cos(\omega_0\tau) - B'\sin(\omega_0\tau)) \\ \gamma(B\cos(\omega_0\tau) - G\sin(\omega_0\tau)) \\ \gamma(B'\cos(\omega_0\tau) + G'\sin(\omega_0\tau)) \end{bmatrix}^T \begin{bmatrix} \delta\phi(t) \\ \delta\dot{\phi}(t) \\ \delta U(t) \\ \delta\dot{U}(t) \\ \delta\phi(t-\tau) \\ \delta\dot{\phi}(t-\tau) \\ \delta U(t-\tau) \\ \delta\dot{U}(t-\tau) \end{bmatrix} \tag{12}$$

By an abuse of notation, line parameters B, G, B', and G' are given as per-unit quantities in the equation above. Next, we introduce $d_p = \frac{k_p\omega_0}{S_b}$, $d_q = \frac{k_qV_b}{S_b}$, where k_p and k_q denote the per-unit droop gains, and S_b denotes the base apparent power. Then, the closed-loop expressions for the inverter droop dynamics can be restated as:

$$\delta\dot{\phi}(t) \approx \delta\omega(t)$$
$$\sigma\delta\dot{\omega}(t) \approx -\delta\omega(t) - k_p\omega_0\delta P_{\text{pu}}(t,\tau)$$
$$\sigma\delta\dot{U}(t) \approx -\delta U(t) - k_q\delta Q_{\text{pu}}(t,\tau)$$

Rearranging the closed-loop expressions in a matrix form, we obtain:

$$N_0\dot{z}(t) \approx N_1(\tau)\dot{z}(t-\tau) + M_0(\tau)z(t) + M_1(\tau)z(t-\tau)$$

where: $z(t) := \begin{bmatrix}\delta\phi(t) & \delta\omega(t) & \delta U(t)\end{bmatrix}^T$ and:

$$N_0 = \begin{bmatrix} 1 & 0 & 0 \\ 0 & \sigma & -k_p\omega_0G' \\ 0 & 0 & \sigma - k_qB' \end{bmatrix}$$
$$N_1(\tau) = \begin{bmatrix} 0 & 0 & 0 \\ 0 & 0 & -k_p\omega_0\gamma(G'\cos(\omega_0\tau) - B'\sin(\omega_0\tau)) \\ 0 & 0 & -k_q\gamma(B'\cos(\omega_0\tau) + G'\sin(\omega_0\tau)) \end{bmatrix}$$
$$M_0(\tau) = \begin{bmatrix} 0 & 1 \\ k_p\omega_0\gamma(B\cos(\omega_0\tau) - G\sin(\omega_0\tau)) & k_p\omega_0B' - 1 \\ k_q\gamma(G\cos(\omega_0\tau) + B\sin(\omega_0\tau)) & -k_qG' \end{bmatrix}$$
$$\begin{bmatrix} 0 \\ -k_p\omega_0[G(2-\gamma\cos(\omega_0\tau)) - B\gamma\sin(\omega_0\tau)] \\ -1 + k_q[B(2-\gamma\cos(\omega_0\tau)) + G\gamma\sin(\omega_0\tau)] \end{bmatrix}$$
$$M_1(\tau) = \begin{bmatrix} 0 \\ -k_p\omega_0\gamma(B\cos(\omega_0\tau) - G\sin(\omega_0\tau)) \\ -k_q\gamma(G\cos(\omega_0\tau) + B\sin(\omega_0\tau)) \end{bmatrix}$$
$$\begin{bmatrix} 0 \\ -k_p\omega_0\gamma(B'\cos(\omega_0\tau) + G'\sin(\omega_0\tau)) \\ k_q\gamma(G'\cos(\omega_0\tau) - B'\sin(\omega_0\tau)) \end{bmatrix}$$
$$\begin{bmatrix} 0 \\ k_p\omega_0\gamma(G\cos(\omega_0\tau) + B\sin(\omega_0\tau)) \\ -k_q\gamma(B\cos(\omega_0\tau) - G\sin(\omega_0\tau)) \end{bmatrix}. \tag{13}$$

This differential equation represents a neutral time-delayed system (NTDS) because a delayed argument appears for derivative terms in addition to non-derivative terms, i.e., $N_1(\tau) \not\equiv 0$ and $M_1(\tau) \not\equiv 0$. Time-delayed systems have transcendental characteristic equations and therefore infinitely many characteristic roots, and, in general, an analytical stability assessment is difficult. But numerical techniques are available for stability assessment of NTDS.

C. Delay-Dependent Stability Assessment

One numerical technique for the stability assessment of NTDS is a frequency-domain method called the *direct method* [21]. This method relies on Rekasius substitution:

$$e^{-s\tau} = \frac{1-sT}{1+sT}, \quad s = j\omega, \quad \omega \in \mathbb{R}, \quad \tau > 0, \quad T \in \mathbb{R}$$

which maps the transcendental characteristic polynomial with infinitely many roots:

$$\det\left(sI - A_0(\tau) - [A_1(\tau) + sA_2(\tau)]\,e^{-s\tau}\right) = 0 \tag{14}$$

where $A_0(\tau) = N_0^{-1}M_0(\tau)$, $A_1(\tau) = N_0^{-1}M_1(\tau)$ and $A_2(\tau) = N_0^{-1}N_1(\tau)$, to a rational polynomial with a finite number of roots:

$$\det\left(sI - A_0(T) - [A_1(T) + sA_2(T)]\,\frac{1-sT}{1+sT}\right) = 0. \tag{15}$$

By an abuse of notation we use matrices A_i but express them as a function of T instead of τ in (15). This change in variables in A_i, which is also due to the Rekasius substitution, will be made explicit in the sequel. Note that the Rekasius substitution is performed only for roots on the imaginary axis, and it is an *exact* substitution, not an approximation. The goal is not to calculate a complete set of roots (as there are infinitely many) but to calculate imaginary axis roots from which stability-instability transitions can be inferred. Rekasius substitution reparametrizes the complex exponential (unit circle) that has angle $-\omega\tau$ so that it is expressed as a rational polynomial in $s = j\omega$ of degree 1 with coefficients in T. The direct method was originally applied to a class of systems for which matrices A_i are constant. Nevertheless, the method can be extended in a straightforward way by performing the following substitutions in matrices $A_i(\tau)$ because dependence on τ in (13) is only through trigonometric functions:

$$\cos(\omega_0\tau) = \frac{1-\omega_0^2T^2}{1+\omega_0^2T^2} \quad \text{and} \quad \sin(\omega_0\tau) = \frac{2\omega_0 T}{1+\omega_0^2T^2}$$

which are obtained by taking the real and the imaginary parts of the Rekasius substitution and evaluating at $\omega = \omega_0$. This way, the polynomial coefficients in (15) can be obtained as functions of T only.

Then, the imaginary axis roots of (15), which are expressed in terms of T, are precisely those of (14), which are expressed in terms of τ. Because roots are continuous functions of the polynomial coefficients and thus delay τ, we are only interested in detecting the imaginary axis roots as their existence indicates a crossing between the left-hand plane and the right-hand plane, i.e., a transition between the stable and the unstable regions. For any imaginary axis root (frequency ω), the following relationship holds due to the Rekasius substitution:

$$\tau = \frac{2}{\omega}\left[\tan^{-1}(\omega T) + l\pi\right] \tag{16}$$

where l is any integer such that $\tau > 0$. Using (16), the critical delay value for which the system undergoes a stability transition can be recovered; therefore, critical frequencies and positive delay values for all stability transitions for a given system, whether the system is delay-free stable or not, can be computed using the direct method. For HIL purposes, we are only interested in the system being delay-free stable and computing the smallest positive delay value that would destabilize the system; therefore, we seek the smallest l value such that $\tau > 0$ in (16) for any candidate pair of ω and T.

We implement direct method based on the procedural steps given in [21], to which the reader should refer for further details. Evaluating (15) leads to a 6^{th}-order polynomial equation in s where the real coefficients are polynomials in T. The polynomial equation is then immediately reduced to a 5^{th}-order by eliminating the trivial root at $s = 0$ (a marginally stable pole due to the phase angle drift). Then, the first column of a Routh array is constructed using coefficients of the polynomial in s, which yields rational polynomials in T as array entries. Because the number of sign changes on the first column of a Routh array equals the number of right-hand plane poles, any real zero of array entries (as rational polynomials reduced to the lowest terms) is a candidate value for T for which there is an imaginary axis crossing (recall that $T \in \mathbb{R}$). For each candidate T value, the imaginary axis roots of (15) are computed, resulting in pairs (ω, T) that lead to a critical positive-delay value computed via (16). Noting again that we assume delay-free stability, we then take the minimum over all (ω, T) pairs of the critical positive-delay values for which system undergoes a stability transition. This value is the smallest destabilizing positive-delay value.

D. Numerical Results

Parameter values used in numerical calculations, which are typical values drawn from the literature, are given in Table I. We choose a value of the feedback parameter γ based on the equilibrium values of power (see Appendix C for details). For four scenarios in which inductance values are an order of magnitude apart; and for a scenario with no inductance, we numerically calculate the smallest critical positive-delay value that destabilizes a delay-free-stable system for various values of per-unit droop gain pair (k_p, k_q). Each scenario is given as a color map in figs. 6b to 6f. The particular region of (k_p, k_q) is defined in each scenario based on the delay-free stability regions given for various inductance values in Figure 6a.

Some notable observations from Figure 6a are as follows. For $L \in \{2\times10^{-5}, 10^{-4}, 10^{-3}, 10^{-2}\}$ mH, the delay-free stability regions monotonically shrink as the inductance value increases. The boundary of these regions allows for an arbitrarily large value for one droop gain for a sufficiently small value of (at the expense of) the other droop gain. This behavior is more pronounced for larger inductance values in this set. These relatively small values of inductance result in unbounded delay-free stability regions, whereas at $L = 10^{-1}$ mH, the stability region is the smallest relative to that of all other scenarios in Figure 6a and is a bounded one. Beyond this inductance value, specifically for $L \in \{1, 1.1\}$ mH, bounded stability regions monotonically grow. The smallest stability region is induced by a value of L, which is in the neighborhood of 10^{-1} mH. Typical values of per-unit droop gains k_p and k_q are on the order of 10^{-3} and 10^{-2}, respectively [22]; therefore, stability margins for the scenario of $L = 10^{-1}$ mH (or smaller) could be limiting for HIL experiments. It could be argued that $L < 10^{-2}$ mH suffices in the absence of a delay, but as will be shown in the sequel, a sufficiently large inductance is needed to improve the stability margins of delayed operation. A line inductance of $L = 1$ mH, which is only one order of magnitude larger than the value that gives the smallest stability region, is chosen for the experimental setup, which, per the numerical calculations, can provide a sufficient stability margin for delay-free operation.

Each color map in figs. 6b to 6f contains empty regions for sufficiently small values of droop gains. These regions contain points (k_p, k_q) for which the system is *delay-independent* stable, i.e., a delay-free stable system (stable for $\tau = 0$) is stable for any $\tau > 0$. For the inductance value $L = 1$ mH that is used in the experiments, this delay-independent stable region in Figure 6b, which is upper bounded approximately at voltage droop gain $k_q = 0.6$ pu (an order of magnitude larger

than typical values) and frequency droop gain $k_p = 0.3$ pu (two orders of magnitude larger than typical values), provides a practically more useful operating region than that of other scenarios. Particularly, for $L = 10^{-1}$ mH, the delay-independent stable region upper bound is around $k_q = 0.2$ pu, as shown in Figure 6c with $k_p < 0.02$ pu. Figures 6d to 6f indicate for the respective values of $L \in \{10^{-2}, 10^{-3}, 0\}$ mH that this upper bound is around $k_q = 0.04$ pu (an order of magnitude smaller than that of the case $L = 1$ mH) for k_p on the order of 0.01 pu, unless the frequency droop gain is reduced to $k_p < 0.01$ pu. These observations suggest that a larger inductance value provides delay robustness from the perspective of achieving a larger delay-independent stable region. Particularly for droop gains $k_p < 0.3$ pu and $k_q < 0.6$ pu, the upper bounds of which are at least an order of magnitude larger than the typical values, $L = 1$ mH provides delay-independent stability. This is the primary benefit of using this inductance value in the experiments.

In fact, the delay-independent stable region for $L = 1$ mH in Figure 6b covers the entire region in Figure 6c for $L = 10^{-1}$ mH and the regions defined by $k_q < 0.6$ pu in figs. 6d to 6f for the respective inductance values of $L \in \{10^{-2}, 10^{-3}, 0\}$ mH. In other words, $L = 1$ mH ensures delay-independent stability for the practical gain values for which smaller inductance values lead to a critical destabilizing value of delay. Outside this region, Figure 6b shows that for 0.6 pu $< k_q < 1$ pu, $L = 1$ mH produces critical delay values satisfying approximately 0.031 ms $< \tau < 2.5$ ms. In the same k_q interval, for $k_p > 0.01$ pu, inductance values $L \in \{10^{-2}, 10^{-3}, 0\}$ mH lead to respective critical delay values of $\tau \in \{0.2, 0.067, 0.054\}$ ms, and for $k_p < 0.01$ pu, these inductance values lead to delay-independent stability, as shown in figs. 6d to 6f. The most restrictive range of critical delay values that $L = 1$ mH produces is at the boundary of the delay-independent and delay-dependent stability regions in Figure 6b (counterintuitively for relatively smaller droop gains), which is 0.031 ms $< \tau < 0.5$ ms. The smallest critical delay value in this range is inferior to $\tau = 0.2$ ms, which $L = 10^{-2}$ mH produces (for 0.6 pu $< k_q < 1$ pu and $k_p > 0.01$ pu) by an order of magnitude, but it is comparable to the values induced by $L \in \{10^{-3}, 0\}$ mH. Further, in Figure 6b ($L = 1$ mH), the critical delay on the delay-independent/delay-dependent stability region boundary mostly attains values on the order of hundreds of μs, which is comparable to or better than the critical delay values of $\tau \in \{0.2, 0.067, 0.054\}$ ms produced by $L \in \{10^{-2}, 10^{-3}, 0\}$ mH (for 0.6 pu $< k_q < 1$ pu, and $k_p > 0.01$ pu), as shown in figs. 6d to 6f; therefore, for relatively large droop gains $k_p > 0.01$ pu and $k_q > 0.6$ pu (at least one order of magnitude larger than typical values), $L = 1$ mH still performs comparably to the smaller inductance values $L \in \{10^{-2}, 10^{-3}, 0\}$ mH. $L = 1$ mH underperforms only if $k_p < 0.01$ pu and $k_q > 0.6$ pu, which leads to delay-independent stability for smaller inductance values of $L \in \{10^{-2}, 10^{-3}, 0\}$ mH. Yet, this operating region would be less common because it requires the voltage droop gain to attain values that are an order of magnitude larger than typical; whereas the frequency droop gain is limited to typical values, which would imply larger reactive power deviations with respect to nominal compared to those of real power.

Parameter	Description	Value
V_b	Base RMS dq-voltage magnitude	270 V
S_b	Base apparent power	10 kVA
ω_0	Nominal frequency	120π rad/s
σ^{-1}	Power measurement filter frequency	12π rad/s
R	Line resistance	0.073 Ω
L	Line inductance	$\{0, 10^{-3}, 10^{-2}, 10^{-1}, 1\}$ mH
γ	Feedback constant	0.5

TABLE I: Parameter values for numerical calculations

The ranges of critical destabilizing delay values are comparable in all scenarios. For larger values of inductance $L \in \{1, 10^{-1}\}$ mH, the most restrictive critical delay value emerges for relatively smaller values of voltage droop gain k_q, as shown in figs. 6b and 6c. This critical delay value then improves for larger k_q before it degrades again, as the boundary of delay-free stability regions are approached (see Figure 6a). In contrast, critical delay values induced by smaller values of inductance $L \in \{10^{-2}, 10^{-3}, 0\}$ mH are most restrictive for larger values of voltage droop gain k_q, and they improve for smaller values of this gain, as shown in figs. 6d to 6f. We note that critical delay values are relatively more sensitive to voltage droop gain, k_q, than to frequency droop gain, k_p, for all scenarios, which could be due to our simplifying assumption of using a real feedback constant, e.g., stronger dependence on voltage magnitude dynamics; however, delay-independent stability regions are still sensitive to frequency droop gain, k_p, for smaller values of inductance $L \in \{10^{-2}, 10^{-3}, 0\}$ mH, as shown in figs. 6d to 6f.

Although $L = 1$ mH provides the highest degree of robustness via a large delay-independent stability region, smaller inductance values can also be sufficient, depending on the application and keeping in mind the associated stability margin deficit. For example, $k_q < 0.2$ pu and $k_p < 0.02$ pu, which allows droop gains of one order of magnitude larger than typical, is a delay-independent stability region in Figure 6c for $L = 10^{-1}$ mH; however, upper bounds of the delay-free stability region in this scenario are also on the same order (see Figure 6a), which is more restrictive than that of $L \in \{1, 10^{-2}, 10^{-3}, 0\}$ mH. An almost full range of critical destabilizing delay values in scenarios of $L \in \{10^{-2}, 10^{-3}, 0\}$ mH is contained in the region $k_q < 0.2$ pu and for k_p on the order of 0.01 pu. For these smaller inductance values, for example, critical delay values of 1 ms or better can be achieved for voltage droop gain $k_q < 0.06$ pu (allows up to typical values), or 0.6 ms or better can be achieved for $k_q < 0.1$ pu (allows up to one order of magnitude larger than typical), whereas the frequency droop gain can be chosen as large as on the order of 0.01 pu (one order of magnitude larger than typical). Noting that the simulation delay is approximately $0.05 - 0.1$ ms, well-tuned lag compensation can manage delays.

VI. Experimental Results

This section presents the PHIL experimental results. First, we present the results from controlling the grid emulator voltage using the resonant tracking controller. Then, we present the results from operating the inverter under GFM and GFL modes of operation depending on the microgrid mode.

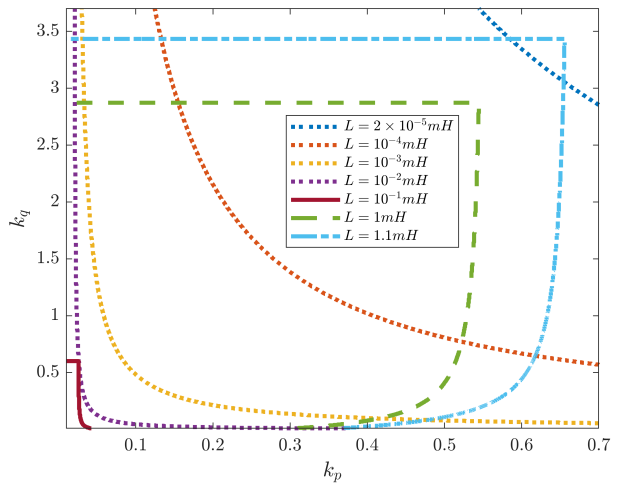

(a) Delay-free ($\tau = 0$)

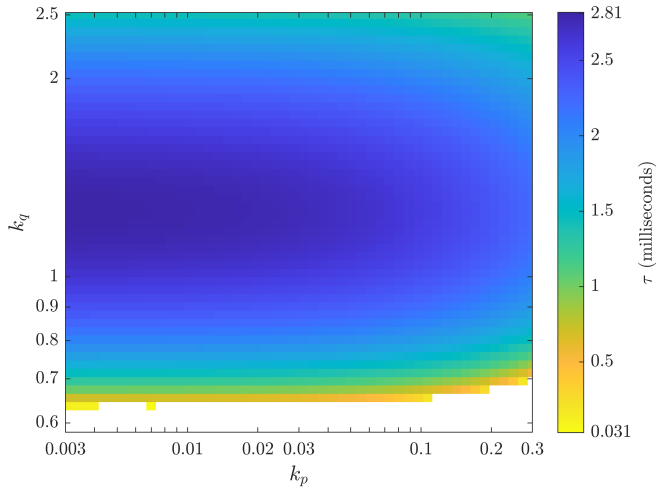

(b) $L = 1$ mH

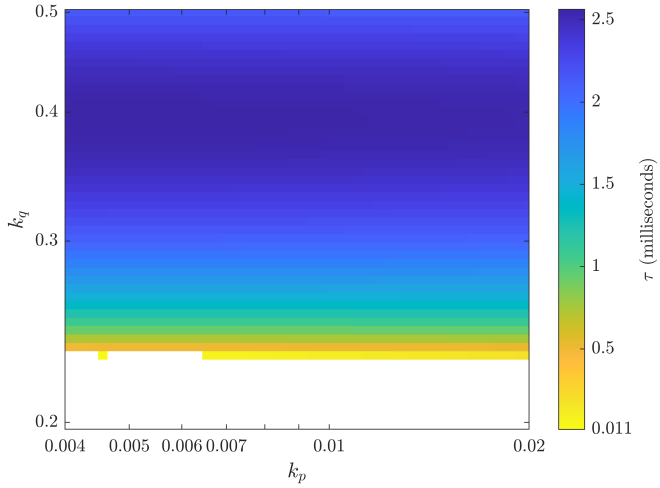

(c) $L = 10^{-1}$ mH

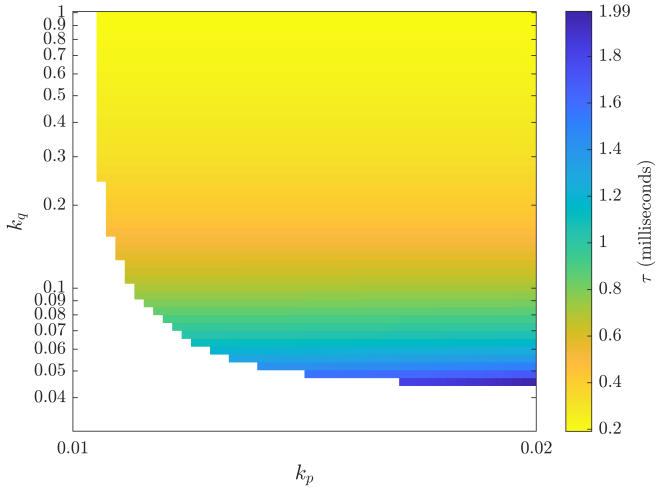

(d) $L = 10^{-2}$ mH

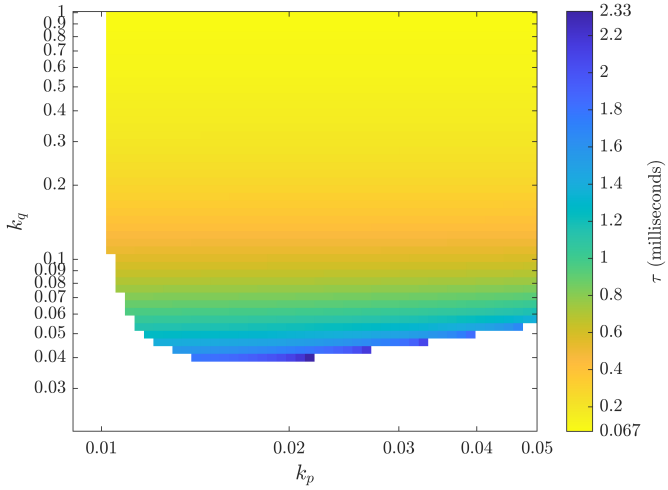

(e) $L = 10^{-3}$ mH

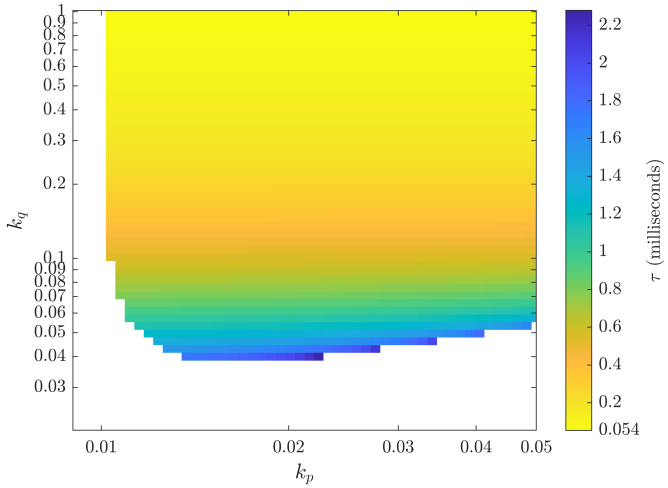

(f) $L = 0$ mH

Fig. 6: (a) Delay-free stability regions for various inductance values. (b–f) Color map of critical destabilizing positive-delay values for each scenario with a different inductance value. Empty regions in the color maps indicate delay-independent stability, i.e., a delay-free stable (stable for $\tau = 0$) system is stable for any $\tau > 0$.

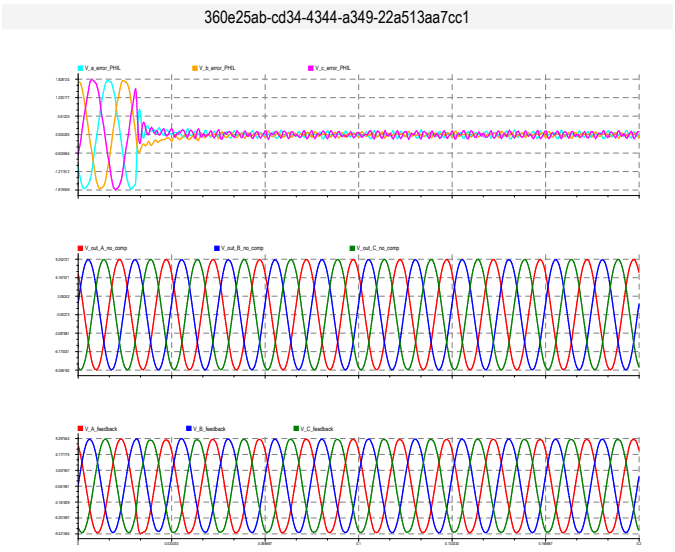

Fig. 7: Operation of the grid simulator with the error minimized when the proportional resonant controller is activated

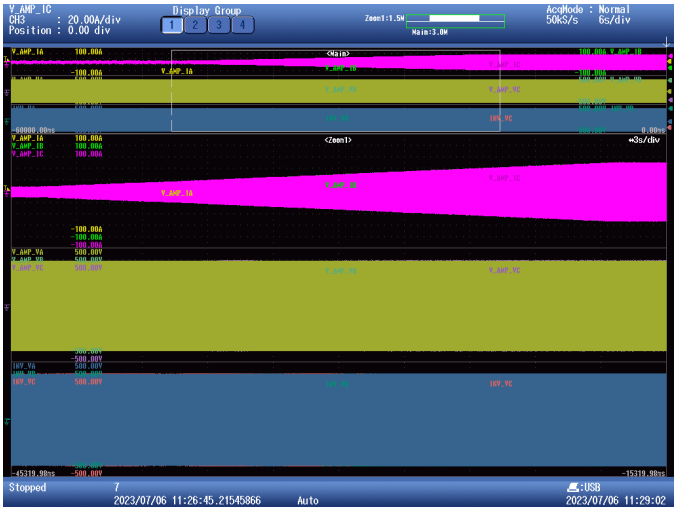

Fig. 8: Grid-connected dispatch

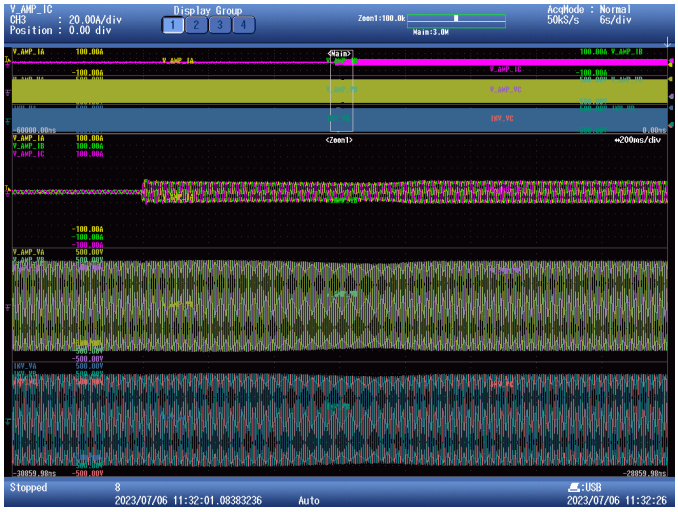

Fig. 9: Transition of microgrid from grid-connected mode to islanded mode. The inverter transitions from GFL mode to GFM mode.

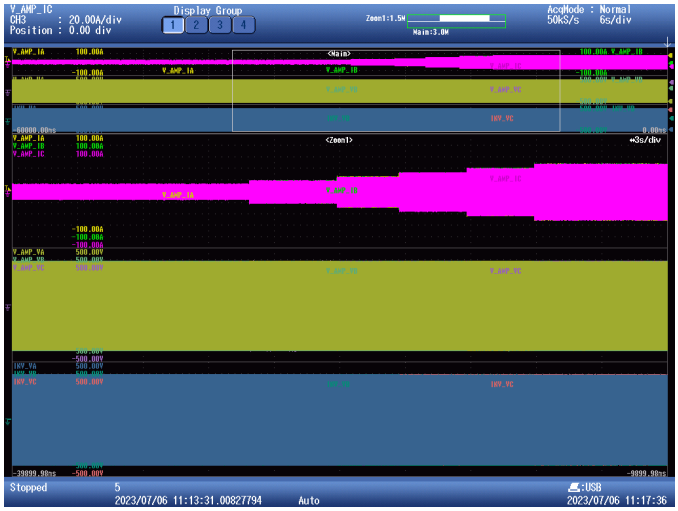

Fig. 10: Islanded dispatch—inverter in GFM mode supporting loads in the microgrid (microgrid is is islanded mode)

A. *Voltage Tracking*

Figure 7 shows three waveforms. The first waveform is the voltage feedback, the second shows the voltage set point, and the third shows the voltage error. Before the resonant controller is turned on, the grid simulator is not following the voltage set point. After turning on the resonant controller, the grid simulator can track the voltage, and the tracking error is significantly reduced.

B. *Power Tracking*

Grid-connected dispatch with inverter in GFL mode: Figure 8 shows the results from grid-connected dispatch with the inverter in GFL mode of operation.

Grid-connected mode to islanded mode with inverter transitioning from GFL to GFM mode: Figure 9 shows the results when the microgrid transitions from grid-connected mode to islanded mode. During this transition, the inverter switched from GFL mode to GFM mode.

Islanded mode of operation with inverter in GFM mode of operation: Figure 10 shows the results when the microgrid is in islanded mode of operation. In islanded mode, loads in the microgrid were increased in steps. The inverter operated in GFM mode and supported the load steps.

Grid resynchronization transition with inverter transitioning from GFM mode to GFL mode: Figure 10 shows the results when the microgrid transitions from islanded mode to grid-connected mode of operation. During this transition, the inverter transitions from GFM mode to GFL mode of operation.

VII. Conclusion

This paper addressed challenges of ensuring the stability of GFM PHIL tests under dynamic conditions; via the use of lead

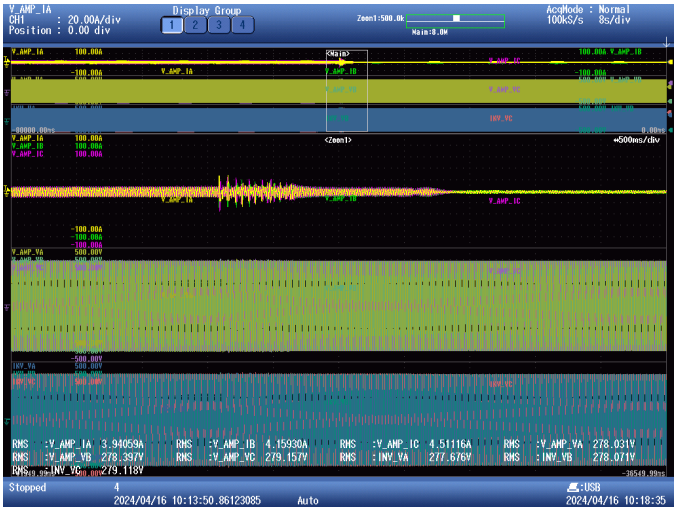

Fig. 11: Transition of microgrid from islanded mode to grid-connected mode. The inverter transitions from GFM mode to GFL mode.

compensation and resonant tracking control schemes as well as the appropriate choice of PHIL interconnection parameter values. These challenges, particularly pertaining to loop delays and destabilizing dynamic modes of PHIL interconnections, have been analyzed using analytical models and numerical simulations. The efficacy of our delay compensation and tracking control approaches have been demonstrated in PHIL experiments at high power (100 kVA GFM inverter) and in various dynamic modes.

ACKNOWLEDGMENTS

This work was authored in part by the National Renewable Energy Laboratory for the U.S. Department of Energy (DOE) under Contract No. DE-AC36-08GO28308 and the National Institute of Standards and Technology. Funding for the NREL author provided by the U.S. Department of Energy Office of Energy Efficiency and Renewable Energy Hydrogen and Fuel Cell Technologies Office. The views expressed in the article do not necessarily represent the views of the DOE or the U.S. Government. Certain commercial entities, equipment, or materials may be identified in this document to describe an experimental procedure or concept adequately. Such identification is not intended to imply recommendation or endorsement by the National Institute of Standards and Technology, nor is it intended to imply that the entities, materials, or equipment are necessarily the best available for the purpose. The U.S. Government retains and the publisher, by accepting the article for publication, acknowledges that the U.S. Government retains a nonexclusive, paid-up, irrevocable, worldwide license to publish or reproduce the published form of this work, or allow others to do so, for U.S. Government purposes.

Official contribution of the National Institute of Standards and Technology; not subject to copyright in the United States. Certain commercial equipment, instruments, or materials are identified in this paper to specify the experimental procedure adequately. Such identification is not intended to imply recommendation or endorsement by the National Institute of Standards and Technology, nor is it intended to imply that the materials or equipment identified are necessarily the best available for the purpose. Parts of this paper may have been presented in technical seminars and included in government publications. Recorded versions of those seminars and copyright free versions of publications are available at https://www.nist.gov/publications.

REFERENCES

[1] RAPA NERC, "2021 Long-Term Reliability Assessment," reliability Assessment, NERC, Dec. 2021.

[2] A. Yazdani and R. Iravani, *Voltage-sourced converters in power systems: modeling, control, and applications*. Hoboken, N.J: IEEE Press/John Wiley, 2010. OCLC: ocn319499984.

[3] R. Teodorescu, M. Liserre, and P. Rodriguez, *Grid converters for photovoltaic and wind power systems*. Chichester, West Sussex: Wiley, 2011.

[4] S. Golestan, J. M. Guerrero, and J. C. Vasquez, "Three-Phase PLLs: A Review of Recent Advances," *IEEE Transactions on Power Electronics*, vol. 32, pp. 1894–1907, Mar. 2017.

[5] NERC, "1 ,200 MW Fault Induced Solar Photovoltaic Resource Interruption Disturbance Report," event Analysis, North American Electric Reliability Corporation (NERC), Atlanta, GA, June 2017.

[6] Y. Lin, J. Eto, B. Johnson, J. Flicker, R. Lasseter, H. Villegas Pico, G.-S. Seo, B. Pierre, and A. Ellis, "Research Roadmap on Grid-Forming Inverters," Tech. Rep. NREL/TP–5D00-73476, 1721727, MainId:6978, NREL, Nov. 2020.

[7] G. Lauss, M. O. Faruque, K. Schoder, C. Dufour, A. Viehweider, and J. Langston, "Characteristics and Design of Power Hardware-in-the-Loop Simulations for Electrical Power Systems," *IEEE Transactions on Industrial Electronics*, vol. 63, pp. 406–417, Jan. 2016.

[8] B. M. Wilamowski and J. D. Irwin, *The industrial electronics handbook. Control and mechatronics*. Boca Raton, FL: CRC Press, 2nd ed ed., 2011. OCLC: 723940296.

[9] X. Guillaud, M. O. Faruque, A. Teninge, A. H. Hariri, L. Vanfretti, M. Paolone, V. Dinavahi, P. Mitra, G. Lauss, C. Dufour, P. Forsyth, A. K. Srivastava, K. Strunz, T. Strasser, and A. Davoudi, "Applications of Real-Time Simulation Technologies in Power and Energy Systems," *IEEE Power and Energy Technology Systems Journal*, vol. 2, pp. 103–115, Sept. 2015.

[10] J. Montoya, R. Brandl, K. Vishwanath, J. Johnson, R. Darbali-Zamora, A. Summers, J. Hashimoto, H. Kikusato, T. S. Ustun, N. Ninad, E. Apablaza-Arancibia, J.-P. Bérard, M. Rivard, S. Q. Ali, A. Obushevs, K. Heussen, R. Stanev, E. Guillo-Sansano, M. H. Syed, G. Burt, C. Cho, H.-J. Yoo, C. P. Awasthi, K. Wadhwa, and R. Bründlinger, "Advanced Laboratory Testing Methods Using Real-Time Simulation and Hardware-in-the-Loop Techniques: A Survey of Smart Grid International Research Facility Network Activities," *Energies*, vol. 13, p. 3267, June 2020.

[11] A. Haddadi, M. Zhao, I. Kocar, U. Karaagac, K. W. Chan, and E. Farantatos, "Impact of Inverter-Based Resources on Negative Sequence Quantities-Based Protection Elements," *IEEE Transactions on Power Delivery*, vol. 36, pp. 289–298, Feb. 2021.

[12] W. Ren, M. Steurer, and T. L. Baldwin, "An effective method for evaluating the accuracy of power hardware-in-the-loop simulations," *IEEE Transactions on Industry Applications*, vol. 45, no. 4, pp. 1484–1490, 2009.

[13] P. Kundur, "Power system stability," *Power system stability and control*, vol. 10, pp. 7–1, 2007.

[14] P. Vorobev, P.-H. Huang, M. Al Hosani, J. L. Kirtley, and K. Turitsyn, "High-fidelity model order reduction for microgrids stability assessment," *IEEE Transactions on Power Systems*, vol. 33, no. 1, pp. 874–887, 2018.

[15] Y. A.-R. I. Mohamed, "Mitigation of dynamic, unbalanced, and harmonic voltage disturbances using grid-connected inverters with *lcl* filter," *IEEE Transactions on Industrial Electronics*, vol. 58, no. 9, pp. 3914–3924, 2011.

[16] N. Ainsworth, A. Hariri, K. Prabakar, A. Pratt, and M. Baggu, "Modeling and compensation design for a power hardware-in-the-loop simulation of an AC distribution system," in *2016 North American Power Symposium (NAPS)*, (Denver, CO, USA), pp. 1–6, IEEE, Sept. 2016.

[17] K. Prabakar, B. Palmintier, A. Pratt, A. Hariri, I. Mendoza, and M. M. Baggu, "Improving the Performance of Integrated Power-Hardware-in-the-Loop and Quasi-Static Time-Series Simulations," *IEEE Transactions on Industrial Electronics*, pp. 1–1, 2020. Conference Name: IEEE Transactions on Industrial Electronics.

[18] {IEEE PEL/SC}, "Hardware-in-the-Loop (HIL) Simulation Based Testing of Electric Power Apparatus and Controls," Standard {P2004}, I, Mar. 2017.

[19] R. Teodorescu, F. Blaabjerg, M. Liserre, and P. Loh, "Proportional-resonant controllers and filters for grid-connected voltage-source converters," *IEE Proceedings - Electric Power Applications*, vol. 153, pp. 750–762, 2006.

[20] W. Michiels, "Control of linear systems with delays," in *Encyclopedia of Systems and Control* (J. Baillieul and T. Samad, eds.), pp. 1–7, London: Springer London, 2019.

[21] N. Olgac and R. Sipahi, "A practical method for analyzing the stability of neutral type lti-time delayed systems," *Automatica*, vol. 40, no. 5, pp. 847–853, 2004.

[22] N. Pogaku, M. Prodanovic, and T. C. Green, "Modeling, analysis and testing of autonomous operation of an inverter-based microgrid," *IEEE Transactions on Power Electronics*, vol. 22, no. 2, pp. 613–625, 2007.

APPENDIX
DERIVATIONS USED IN SECTION V

A. Proof of Claim in Assumption 1

Let us denote the mapping from the GFM inverter voltage to the simulated load-side voltage by F_{21}. We use the notation given in Figure 5 to write:

$$F_{21}(s) = \frac{v_2(s)}{v_1(s)} = \frac{sL_l + j\omega_0 L_l + R_l}{sL_a + j\omega_0 L_a + R_a} = \left(\frac{R_l}{R_a}\right) \frac{s\frac{L_l}{R_l} + j\omega_0 \frac{L_l}{R_l} + 1}{s\frac{L_a}{R_a} + j\omega_0 \frac{L_a}{R_a} + 1}$$

where $R_a = R_s + R_l$ and $L_a = L_s + L_l$, subscript 's' denotes the simulated line impedance, and subscript 'l' denotes the simulated load impedance parameters. $F_{21}(s)$ can be simplified for specific parameter values. For $\epsilon > 0$, consider:

$$\left|\frac{L_a}{R_a} - \frac{L_l}{R_l}\right| = \left|\frac{L_s R_l - L_l R_s}{R_l^2 + R_l R_s}\right| < \epsilon$$

$$\Leftrightarrow \quad \left|\frac{L_s}{R_s} - \frac{L_l}{R_l}\right| < \epsilon\left(\frac{R_l}{R_s} + 1\right) =: \rho(\epsilon)$$

if $R_l \neq 0$ and $R_s \neq 0$. Then, as $\epsilon \to 0$, $\frac{L_s}{R_s} \to \frac{L_l}{R_l}$ for a given $\frac{R_l}{R_s}$ if and only if $\frac{L_a}{R_a} \to \frac{L_l}{R_l}$. Put another way, for similar inductance-to-resistance ratios of load and simulated line, i.e. $\frac{L_s}{R_s} \to \frac{L_l}{R_l}$, and given $\frac{R_l}{R_s}$, one can find $\rho(\epsilon) \to 0$ such that $\left|F_{21}(s) - \frac{R_l}{R_a}\right| \to 0$; therefore, $v_2 \approx \gamma v_1$ and $\gamma = \frac{R_l}{R_a}$.

B. Linearized Variables

Based on Assumption 1, we consider $v_2(t) = \gamma v_1(t)$, where these voltages are dq coordinate phasors as before. We assume $\phi_{12}^* = 0$ for a zeroth-order approximation with respect to the equilibrium angle difference:

$$V_2^* = \gamma V_1^* e^{j\phi_{12}^*} = \gamma V_1^*.$$

Linearized dq phasor voltages satisfy $\delta v_2 \approx \gamma \delta v_1$, which leads to:

$$(\delta V_2 + jV_2^* \delta\phi_2) \approx \gamma e^{j\phi_{12}^*}(\delta V_1 + jV_1^* \delta\phi_1).$$

Then, using $\phi_{12}^* = 0$ and $V_2^* = \gamma V_1^*$ reduces the expression above to:

$$\delta V_2 \approx \gamma \delta V_1 \quad \text{and} \quad \delta\phi_2 \approx \delta\phi_1.$$

C. Equilibrium Power With Respect to Feedback Parameter

Complex power based on dq phasor parameters can be expressed as $p_1 = v_1(i_{12})^H$ which at equilibrium leads to (assuming $\phi_{12}^* \approx 0$):

$$p_1^* \approx ((V_1^*)^2 - V_1^* V_2^*) y_{12}^H = (1-\gamma)(V_1^*)^2 y_{12}^H.$$

as the power injected by the inverter. Similar calculations give:

$$p_2^* \approx ((V_2^*)^2 - V_2^* V_1^*) y_{12}^H = -(1-\gamma)\gamma(V_1^*)^2 y_{12}^H$$

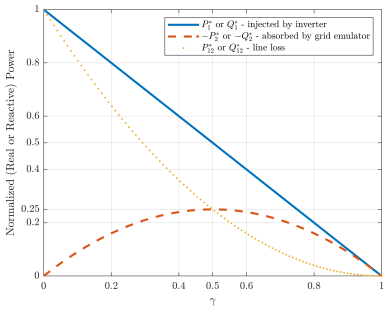

Fig. 12: Normalized power at equilibrium with respect to the feedback parameter

where $-p_2^*$ would be the equilibrium power absorbed by the grid emulator, and the line loss would be:

$$p_{12}^* \approx (V_1^* - V_2^*)^2 y_{12}^H = (1-\gamma)^2 (V_1^*)^2 y_{12}^H.$$

Recall that $0 < \gamma < 1$. We use $\gamma = 0.5$ in numerical calculations because this value provides an operating point at which the power injected by the inverter is maximally absorbed by the grid emulator, as shown Figure 12.